International Journal of Material Forming (2022) 15: 4
https://doi.org/10.1007/s12289-022-01654-y

DEVELOPMENTS IN MODELLING AND SIMULATION..JAPAN, SOUTH KOREA AND CHINA

Analyses of shearing mechanism during shear-cutting of 980 MPa dual-phase steel sheets using ductile fracture modeling and simulation

Shamik Basak[1] · Chanyang Kim[2] · Youn Il Jung[3] · Hong-Kyo Jin[4] · Myoung-Gyu Lee[2]

Received: 17 June 2021 / Accepted: 10 January 2022 / Published online: 28 January 2022

Abstract
In this work, the effects of various process input parameters in the sheared edge characteristics are studied during shear-cutting of DP980 sheet material. A virtual experimental approach, based on finite element (FE) modeling of the trimming process, is used to investigate the shearing mechanism precisely. In this context, the Hosford–Coulomb (HC) fracture model is used to predict the fracture initiation, and a hybrid experimental-numerical technique is adopted to calibrate HC parameters. Furthermore, the calibrated HC model is incorporated into FE simulation of the shear-cutting process. Experimental sheet trimming setup is also developed to conduct the experiments, and subsequently validate the developed FE models. It is found that the sheared edge quality and trimming load are varied by the process parameters including trimming angle, trimming clearance and punch radius. Therefore, regression models are proposed to understand the effect on the sheared edge profile and trimming load while varying the input parameters simultaneously. Subsequently, these regression models are represented in the 3D space as a function of the input parameters to visualize the tendency of variations of process parameters on outputs over the operating range. The mathematical models are useful to predict and subsequently improve sheared edge quality by varying the process parameters. Furthermore, a comparison between the open-cut and close-cut processes has also been studied. Two different crack propagation mechanisms are observed due to difference in the boundary conditions regarding rotation of the scrap. For this reason, a strong variation in the stress triaxiality evolution is observed between two processes.

Keywords Shear-cutting · Ductile fracture model · Sheared edge · Burr · Regression models · Finite element modeling

Introduction

Recently, there is a significant interest in increasing the use of advanced high strength steels (AHSSs) including dual phase (DP) steels, transformation-Induced plasticity (TRIP) steels, etc., in auto body fabrication due to their superior strength and formability with excellent crash energy absorbing behavior. During auto body part fabrication, the shear-cutting process plays an important role [1]. Shear-cutting processes such as blanking, hole-piercing can be considered as the early manufacturing stages to prepare the sheet materials for subsequent forming operations [2]. On the other hand, trimming operation, one of the shear-cutting processes, is extensively used to separate the scrap from the final formed product at the end of the product assembly line [3]. Hence, sheet metal researchers are interested to analyze the quality of the product resulting from the shear-cutting processes.

Shamik Basak and Chanyang Kim contributed equally to this work.

✉ Myoung-Gyu Lee
myounglee@snu.ac.kr

[1] Department of Mechanical and Industrial Engineering, Indian Institute of Technology Roorkee, Roorkee 247667, India

[2] Department of Materials Science and Engineering & RIAM, Seoul National University, 1 Gwanak-ro, Gwanak-gu, Seoul 08826, Republic of Korea

[3] Sheet Metal Development Team, Hyundai Motor Company, 150 Hyundaiyeonguso-ro, Namyang, Hwaseong-si, Gyeonggi-do 18220, Republic of Korea

[4] 4MS Autotech Co. Ltd., Anyang-Si, Gyeonggi-Do 431060, Republic of Korea

The quality of the sheared edge is often determined by the height of the burr produced during shear-cutting processes [4]. Edge cracking is another big setback during the shear-cutting process as it often reduces the formability of the sheet materials [5, 6]. Another problem during cutting is the ripping of small particles from the sheared surface of the finished product as observed by Krinninger et al. [7]. These small particles reduce the quality of the finished components by accumulating on the blank surfaces and cutting edges. It is often observed that after primary trimming, the punch re-strikes the cut surface generating a second sheared surface which is not desirable as it reduces the part quality [8] and giving rise to a secondary peak of load at the end of the primary trimming operation [9]. These defects till discussed are very crucial and can affect the quality of the trimmed products.

It is found that the quality of the sheared surface depends upon the process parameters selected during the cutting process. There were some early studies showed that the shear surface quality and burr height of low/medium carbon steels and commercial aluminum alloys depended upon the tool inclined angle, tool clearance, tool sharpness, and strain rate in terms of changing temperature, edge radii, sheet orientation angle, punch speed, etc. [10–12]. Choi et al. [13] closely observed the effect of clearance and blade angle on the sheared edge quality of AHSS. Chumrum et al. [14] investigated the quality of the piercing hole, load, and energy for three different AHSS materials. Apart from studying the effect of the process parameters, some researchers proposed new technologies to improve the sheared edge quality. So et al. [15] proposed that the effect of temperature improves the sheared surface quality of hot-stamped 22MnB5 steel. Mori et al. [16] used local heating by passing current between the binder and the knockout to increase the quality of the sheared edges of automotive-grade steels.

It is understood from the previous discussions that the trimming quality of the sheet materials depends upon the various process parameters separately. However, during actual trimming operations on the industrial sites, all these process parameters can be varied simultaneously. Moreover, the selection of the proper combination process parameters can able to reduce the defects during shear cutting. As per the current state of the art, the cutting surface characteristics are still unknown while varying all the process parameters simultaneously. Generally, the design of experiment (DOE) method is applied for this purpose in various sheet metal forming problems including incremental forming [17] and hydroforming [18]. Recently, Schenek and Liewald [19] developed regression equations to analyze the cutting surface characteristics during trimming with a slant angle. However, there is still a dearth in literature where some predictive mathematical models will be proposed to predict and subsequently improve the sheared edge quality in prior by varying the input process parameters.

Apart from analytical prediction, numerical analysis of the shear cutting process is often used to predict the quality of the products. Moreover, a virtual experimental approach, based on FE modeling is always preferred as it provides information on the stress state, trimming load, and cutting surface quality, which is difficult to obtain directly from experiments. Traditionally, the forming limit diagram (FLD) is used as a diagnostic tool to predict failure of the sheet metals mainly due to the localized necking during sheet forming processes [20]. However, the ductile damage model described in the stress-strain combined space is used usually to predict fracture during shear-cutting of the sheets. A lot of previous studies were performed to incorporate different classical ductile damage models including McClintock [21], Cockcroft–Latham [22], Oyane [22], and GTN [23] to predict the edge quality and trimming load during the shear-cutting process. Some researchers [24, 25] also compared the predictive efficiency of various damage models to understand the influence of the damage model on cut surface quality prediction. However, there is a recent development in the field of ductile fracture modeling and many coupled/uncoupled fracture models are proposed. Recently proposed advanced ductile fracture models include Hosford–Coulomb (HC) [26], Hu–Chen [27], and Lou–Huh [28]. Sheet metal researchers are now interested to implement advanced fracture models for the prediction of fracture initiation during different sheet metal forming problems [29–31]. Samadian et al. [32] implemented calibrated fracture surface using the GISSMO platform in LS-Dyna to predict the fracture of AHSS. Basak and Panda [33] implemented the advanced yield models into the modified Bao–Wierzbicki (BW) fracture model to predict the fracture during multistage forming experiments.

From the literature studies, it is observed that limited research has been performed on the implementation of advanced fracture models for predicting the cut edge quality during shear-cutting. Moreover, there is little open literature that closely inspects the differences in shearing mechanism during various types of shear-cutting processes of AHSS using FE modeling implementing advanced ductile fracture models. In this study, the Hosford-Coulomb (HC) model, one of the advanced fracture models, is implemented to study the shear quality during the shear-cutting process for DP980 sheets. A hybrid experimental–numerical approach is adopted for the accurate calibration of the HC fracture model. Subsequently, 2D and 3D FE models for trimming in a straight-line path and circular path were developed. An experimental sheet trimming setup was also developed to conduct the experiments and validated the proposed FE models. Further, the effects of various process input parameters including trimming angle, clearance, and punch radius

on the shearing process were studied. Moreover, regression models were developed to correlate the sheared edge characteristics and trimming load with the input process variables. In the end, the shearing mechanism was compared for open-cut and close-cut trimming processes through finite element simulations.

Experimental study

In the present study, cold-rolled DP980 sheets with a nominal thickness of 1.4 mm was considered. Uniaxial tensile test and fracture tests were performed as discussed below.

Uniaxial tensile tests

Uniaxial tensile experiments were performed using an Instron 8801 servo-hydraulic UTM equipped with a load cell of 100 kN capacity. ASTM E8 standard tensile test specimens were used. All the samples were tested at a constant crosshead speed of 3 mm/min, which is quasi-static conditions. Further, tensile tests were performed along with three material directions including 0° (rolling direction, RD), 45° (diagonal direction, DD), and 90° (transverse direction, TD).

Table 1 Mechanical properties of the DP980 sheet material

Orientation	E (GPa)	Y (MPa)	UTS (MPa)	UEL (%)	*r*-value
RD	198.8	658.1	1031.1	11.7	0.843
DD	192.2	650.8	1031.4	12.2	1.095
TD	202.0	655.6	1051.1	11.6	0.966

Three tests were performed for each orientation, respectively. In-plane surface displacement fields were determined using the commercial DIC package VIC-3D (Correlated Solutions Inc.). Virtual extensometers were used to measure engineering strains in loading and transverse directions during the tests. The *r*-values along three anisotropic directions were evaluated by calculating the logarithmic plastic strains along the width and thickness directions assuming plastic incompressibility [20]. The mechanical properties including Young's modulus (E), initial yield stress (Y), ultimate tensile strength (UTS), uniform elongation (UEL), and *r*-values were evaluated and reported in Table 1. It can be observed that DP980 does not exhibit a great anisotropy. Moreover, the normal anisotropy $\left(\bar{r} = \left(r_0 + r_{90} + 2r_{45}\right)/4\right)$ value is 1.0 for this material. Hence, the material response can be considered as isotropic in the constitutive modeling of plasticity.

Fracture tests

Fracture specimens were designed in such a way that it provides information on fracture initiation over a wide range of stress states from pure shear to biaxial tension. It includes notch tension (NT) specimen with a notched radius of 7 mm, plane strain (PS) specimen, specimen with a central hole (CH), and in-plane shear (SH) specimen as shown in Fig. 1a–d, respectively. The NT specimen was designed to measure the fracture strain between uniaxial to biaxial tension zones. Fracture strain near the plane strain region was measured with the PS specimen and the CH specimen was used to determine the fracture strain at uniaxial tension. The hole to ligament width ratio for CH specimen usually plays an important role and it affects the location of the highest

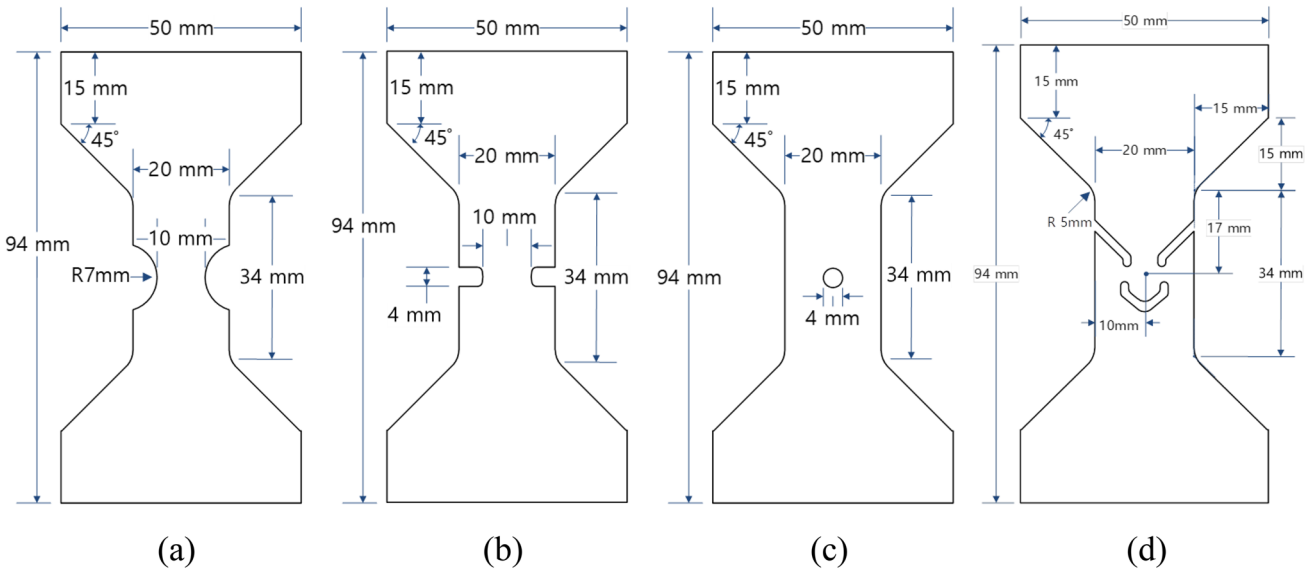

Fig. 1 Schematic of specimen geometries for (**a**) NT, (**b**) PS, (**c**) CH and (**d**) SH specimens

strained point as indicated by various researchers [34–36]. After preliminary tests, the width and hole diameter for the CH sample was fixed as 20 mm and 4 mm, respectively, to ensure the fracture initiation point at the hole edge and the uniaxial stress state up to the onset of the fracture. All the fracture specimens were prepared using the W-EDM along RD. Although the fracture occurs along the through-thickness direction in the trimming process, it is very challenging to investigate the fracture behavior for thickness direction for the sheet metals. Hence, fracture tests were conducted for in-plane conditions, and fracture behavior is assumed as isotropic in the modeling. Three tests were conducted for each type of specimen to ensure the repeatability of the experimental data. All the specimens were tested up to the initiation of the fracture with a constant test speed of 1 mm/min. Deformations in the fracture tests were measured using the commercial DIC package, VIC-3D. A virtual extensometer with a gauge length of 25 mm was used in the longitudinal direction to measure the load-displacement curves during the analyses of fracture tests.

Trimming experiments

A generalized schematic arrangement of the sheet trimming process in a circular path is shown in Fig. 2a. From the cross-sectional view (AA view) it is well understood that the circular trimming process possesses only one axis of symmetry as shown in the figure. Trimming in a straight line path is a special case of the circular trimming process where the punch radius is theoretically infinite. In this work, an experimental setup for a straight trimming process was designed and fabricated to perform the trimming experiments of DP980 material. The arrangements of straight edge punch, binder, blank and die for the trimming experiments are shown in Fig. 2b. A pair of the fixture was fabricated to attach the trimming setup to the UTM of 250 kN capacity. The top and bottom fixtures were attached with the upper and lower jaw of the UTM, respectively. Further, the punch is attached to the top fixture during the experiments. The die and the binder were attached with the bottom fixture as shown in Fig. 2b. The guide rods were positioned to direct the downward movement of the punch fixed with the top fixture during the trimming experiments. A piece of sheet materials of 100 mm × 40 mm dimension was clamped between the binder and the die. The travel speed was taken as 20 mm/min and kept constant during the experiments.

Plasticity and fracture models

Plasticity model

The isotropic Levy-von Mises plasticity model is used to describe the yield behavior of DP980 material. The strain hardening behavior of the sheet material is modeled using the combined Swift-Voce (CSV) hardening curve in Eq. (1).

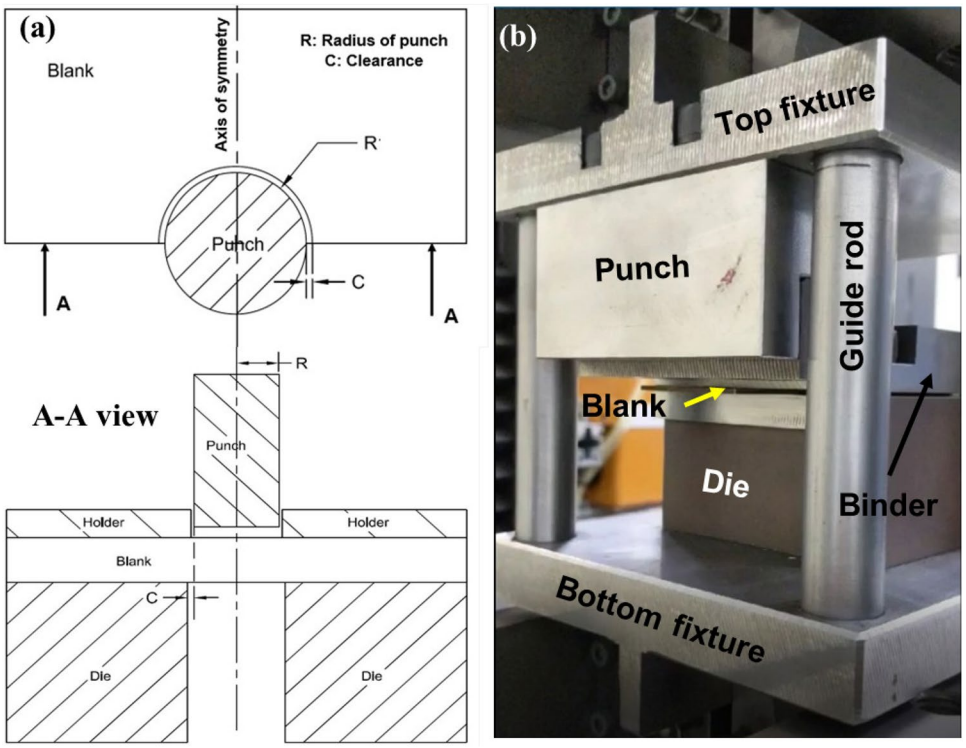

Fig. 2 **a** Schematic diagram of the trimming in a circular path along with the **b** experimental setup for trimming in straight-line path (a special case of circular trimming)

$$\sigma_{CSV} = R\sigma_{Swift} + (1 - R)\sigma_{Voce} \quad (1)$$

Here, σ_{Swift} and σ_{Voce} are the flow stresses corresponding to Swift and Voce hardening model, respectively, which can be represented as follows

$$\sigma_{Swift} = K\left(\varepsilon_0 + \bar{\varepsilon}\right)^n, \sigma_{Voce} = s_0 + s_1\left\{1 - \exp\left(-m_1\bar{\varepsilon}\right)\right\} \quad (2)$$

All the material constants related to CSV hardening law were estimated from the true stress-strain response of the DP980 material and recorded in Table 2. In Eq. (1), R represents a linear combination factor of the Swift and Voce models and the value is between 0 and 1.

Fracture initiation model

Hosford-coulomb ductile fracture model

Mohr and Marcadet [26] proposed the Hosford-Coulomb (HC) fracture criterion to predict the onset of fracture. The effect of non-proportional loading paths is accounted in this model by using a damage indicator (D) framework. The linear damage evolution law can be expressed as

$$D = \int_0^{\bar{\varepsilon}} \frac{d\bar{\varepsilon}}{\bar{\varepsilon}_{f,pro}\left(\eta, \bar{\theta}\right)} \quad (3)$$

In Eq. (3), $D = 0$ signifies the plastically undeformed material and $D = 1$ signifies the onset of ductile fracture of the material. This damage indicator (D) is defined as a linear accumulation of the ratio between the plastic strain increment and the monotonic fracture strain at the given stress states. The stress state of a material can be defined with the stress triaxiality (η) and Lode angle parameter ($\bar{\theta}$) which depends upon the mean stress (σ_m), von Mises equivalent stress ($\bar{\sigma}$), and third stress tensor invariant (J_3).

$$\eta = \frac{\sigma_m}{\bar{\sigma}} \quad (4)$$

$$\bar{\theta} = 1 - \frac{2}{\pi}\arccos\left[\frac{27}{2}\frac{J_3}{\bar{\sigma}^3}\right] \quad (5)$$

In terms of proportional fracture strain, there are two approaches in the HC model. Mohr and Marcadet [26] proposed the HC criterion with a consistent hardening equation that is the same as the plasticity model. Also, a simplified HC model was used that employs the transformation hardening exponent for the practical engineering purpose [37–39]. In this study, the HC model with a consistent hardening is used. In that HC model description, fracture criterion in stress space is described as follows.

$$\bar{\sigma}_f\left(\eta, \bar{\theta}\right) = b\left[\left\{\frac{1}{2}\left((f_1 - f_2)^a + (f_1 - f_3)^a + (f_2 - f_3)^a\right)\right\}^{\frac{1}{a}} + c\left(f_1 + f_3 + 2\eta\right)\right]^{-1} \quad (6)$$

Then, equivalent fracture strain is converted into equivalent fracture strain using an inverse of the hardening law. The trigonometric functions f_{1-3} are the Lode angle parameter dependent functions which are associated with the transformation from principal stresses to the Haigh-Westergaard space as follows

$$f_1 = \frac{2}{3}\cos\left(\frac{\pi}{6}\left(1 - \bar{\theta}\right)\right), \quad (7)$$

$$f_2 = \frac{2}{3}\cos\left(\frac{\pi}{6}\left(3 + \bar{\theta}\right)\right), \quad (8)$$

$$f_3 = -\frac{2}{3}\cos\left(\frac{\pi}{6}\left(1 + \bar{\theta}\right)\right), \quad (9)$$

Then, equivalent fracture strain is converted into equivalent fracture strain using an inverse of the hardening law.

$$\bar{\varepsilon}_f\left(\eta, \bar{\theta}\right) = h^{-1}\left(\bar{\sigma}_f\left(\eta, \bar{\theta}\right)\right) \quad (10)$$

For the Inversion of the combined Swift-Voce law, the Newton-Raphson method was employed. Also, a, b and c are the HC fracture model parameters which are calibrated using a hybrid experimental-numerical technique as discussed below.

Loading paths to fracture

Surface strain during the deformation of the fracture specimens is measured with the DIC system [28]. However, it is difficult to measure the stress and strain field inside the specimens experimentally [35, 40]. Moreover, it is also required to identify the stress-strain response in the post-necking region. Therefore, in this work, a hybrid experimental-numerical technique was adopted to determine the stress and strain field inside the fracture specimens. In this method, the load-displacement curves are obtained from the experiment using DIC or a conventional extensometer. Simultaneously, FE simulations of the fracture tests are performed and the maximum strains (termed as fracture strains)

Table 2 Evaluated combined Swift-Voce hardening parameters for DP980 material

R	K (MPa)	ε_0	n	s_0 (MPa)	s_1 (MPa)	m_1
0.8	1520.2	0.0007	0.119	731.29	410.84	38.33

are identified from simulations corresponding to the experimental fracture stroke. Furthermore, the evolutions of the stresses and equivalent strain are also extracted from the simulation. Then, damage model parameters are optimized using these data.

The FE models of the four different fracture specimens were developed separately, and simulations are performed with Abaqus/standard (implicit scheme). One-quarter symmetric models were generated for NT, PS, and CH specimens, and half symmetric model was generated for SH. The specimens were modeled using reduced integration eight node solid elements (C3D8R) in the Abaqus element library. Also, von Mises yield function was used for the fracture simulations. The CSV hardening curve was used to estimate the stress-strain response of DP980 material. The numerical value of the combination factor R was inversely calibrated based on the FE simulation to obtain the post-UTS hardening of the sheet material. The experimental and simulated load-displacement curve, obtained for NT specimen, is shown in Fig. 3a. The value R was iteratively calibrated, and it was observed that for the $R = 0.8$ the experimental load-displacement curves were predicted precisely. FE simulations were performed with the same value of R for CH, PS and, SH specimens. All the experimental and subsequently predicted load-displacement curves are plotted in Fig. 3b–d for CH, PS, and SH specimens, respectively. The onset of fracture point, obtained from the experiment, is also marked with the red-cross in the corresponding figures. A good agreement between the experimental and predicted curves signifies that the calibrated hardening model able to predict the post-UTS hardening for different fracture specimen of DP980 material. Furthermore, the effective strain contours at the same displacement up to the failure step obtained from FE analyses are shown in the inset of corresponding load-displacement curves in Fig. 3. The color red in the contour indicates the maximum effective strain in each figure. Also, the locations where the maximum effective strain is applied are marked with the red dot in the same figure, and that position was assumed as the fracture initiation point.

Calibration of the HC model

The stress states and effective strain histories of the marked elements (in Fig. 3) were extracted from FE simulation up to the onset of fracture. The evolutions of effective strain with stress triaxiality and Lode angle parameter are shown in Fig. 4a and b, respectively. It can be observed that the stress triaxiality and Lode angle parameter are almost constant for the CH and SH specimens. On the other hand, the stress state is constant up to the onset of necking for NT and PS

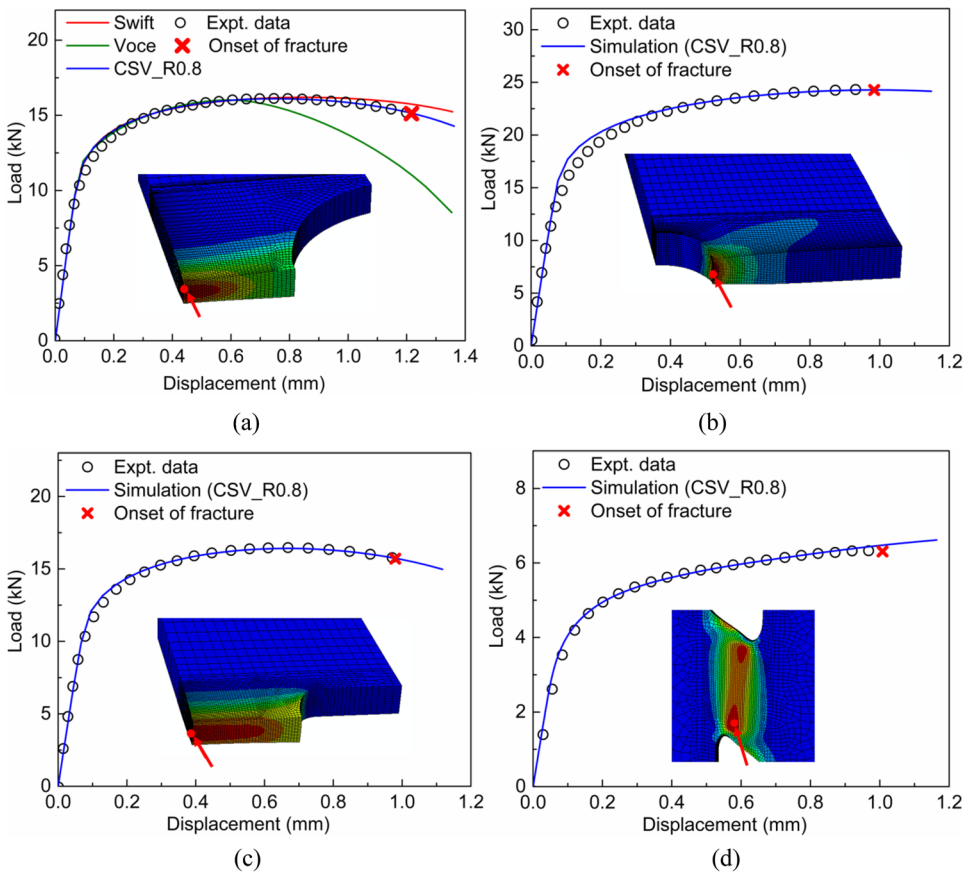

Fig. 3 Comparison of experimental and FE simulated load-displacement curves for (**a**) NT, (**b**) CH, (**c**) PS, and (**d**) SH specimens for DP980 sheet material

specimens, and after that, the stress triaxiality increases with a decrease in the Lode angle parameter due to the localized thickness reduction.

The deformation histories until the fracture are used to optimize the parameters of the HC fracture model. Loading paths of three different fracture specimens including CH, PS, and SH were used to calibrate the unknown model parameters a, b, and c. Optimized HC model parameters are $a = 1.426$, $b = 1444.29$, and $c = 0.0483$. Also, the onset of fractures, estimated with the optimized model, are marked with the black dot in Fig. 4a and b. The prediction of the fracture points for the NT specimen shows a satisfactory agreement with the experimental data. The calibrated HC fracture strain surface of DP980 material is plotted for general stress states space in Fig. 5. In the figure, the fracture strain loci in plane stress conditions are marked with red lines on the 3D surface.

Finite element simulation as a virtual trimming tool

A closer observation of the shearing mechanism is always challenging with direct experiments. Hence, a virtual experimental approach, based on finite element (FE) modeling of the trimming process, was used in the present study. Subsequently, various FE models are prepared to perform the virtual experiments for different trimming conditions. LS-Dyna, the explicit solver, was used in the trimming simulations. During trimming, the sheared surface quality in the through-thickness direction is the prime interest. Therefore, it is sufficient to use a two-dimensional (2D) plane strain FE model for the straight-line cutting. However, to understand the real scenario, it is necessary to analyze the results obtained from the 3D FE model. Moreover, there are various cases where the trimming is not symmetric or trimming can be along a partial circular path (refer to Fig. 2a). These trimming conditions lead to asymmetric boundary conditions, and for that, it is mandatory to use a 3D FE model. Also, 2D plane strain shell element was used for 2D shear-cutting simulation and the 3D solid element was used for all the 3D shear-cutting simulation.

The 2D plane strain model for the straight-line cutting is shown in Fig. 6a. The model was developed in the XY plane and the punch was traveled in the negative Y direction with a predetermined velocity profile. The blank was meshed using 2D plane strain shell elements. The adaptive method of mesh refinement or re-meshing was used to avoid the divergence of the solution due to severe plastic deformation in the localized region. Further, the 3D FE model for straight-line path and circular path are shown in Fig. 6b and c, respectively. All the 3D models were developed in the Hypermesh®. All the tooling such as punch, binder, and die were defined as rigid bodies and only the blanks were elastic-plastic deformable-body. As the DP980 sheet material does not exhibit significant planar anisotropy; hence, the blank materials are assumed to be isotropic. Subsequently, the von Mises yield function along with isotropic hardening was used in the present work. Additionally, the calibrated 3D HC fracture surface was implemented to predict the initiation and propagation of the fracture during trimming. The evaluated fracture surface was incorporated into the FE model through GISSMO (Generalized Incremental Stress State dependent damage MOdel) platform which is available in LS-Dyna. The GISSMO was developed by Neukamm et al. [41] based on incremental damage accumulation and subsequent failure. Finite element deletion was used together with the HC fracture model, or stiffness of the fully damaged (or damage parameter D in Eq. (3) reaches 1) element becomes zero. The GISSMO platform enables to application of the various stress state-dependent fracture models on the FE simulations, with consideration of the non-proportional strain paths based on damage accumulation using plastic strain increment [42]. Detailed information on the GISSMO platform can be referred to [42–45].

Mesh sensitivity analyses

A non-uniform meshing strategy was adopted for meshing the deformable blanks. It is already mentioned that the sheared surface quality along the through-thickness direction is the prime region of interest during trimming. Hence, a thin area of the blank, just below the punch, of 0.5 mm (mentioned as l in Fig. 6b and c) length, is ultra-finely meshed. However, all the other portion of the blank was meshed with coarse size element to decrease the computational time by reducing the number of elements. Furthermore, the XZ symmetry of the blank was used for straight trimming, and half rotational symmetry along the YZ axis was used for circular trimming to reduce the number of elements.

The number of elements in the deforming region in the trimming simulations is critical because plastic deformation occurs at the very narrow region. Also, the elements that reach the critical damage are eroded, and the volume of the blank is reduced due to that element deletion. Hence, mesh sensitivity analyses were performed during 2D FE simulation for the straight cutting by varying mesh size of the deformable blank in different values viz. 5, 10, 15, 20, 30, 40, and 50 µm. For each simulation case, the simulation time (CPU time in hour) and the error in burr height prediction compared to experimental value were evaluated and plotted in Fig. 7a. It can be observed that the accuracy of prediction is within 11% when a mesh size is within 20 µm. However, if the mesh size is larger than 20 µm, the error in burr prediction is significantly increasing. For the mesh size 5 µm, the prediction error is reduced to around 5% with a very

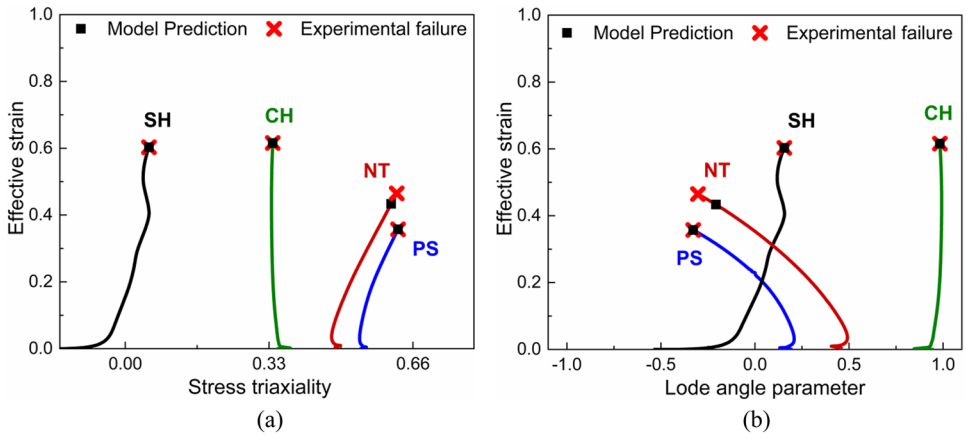

Fig. 4 Effective strain contour plot at the same displacement up to the failure step for NT, CH, PS, SH fracture specimens and the evolution of the effective fracture strain as a function of (**a**) stress triaxiality and (**b**) Lode angle parameter DP980 sheet materials

smooth sheared surface. However, the computation time also increases around 1.7 times for using the ultra-fine meshing of 5 µm. The load-displacement curves for the three different mesh size cases (10, 20, and 30 µm) are shown in Fig. 7b, and compared with the experimental data. It can be observed that the peak loads are comparable for different mesh size cases. However, the displacement is small for coarse mesh size (30 µm) because of the quick propagation of the cracks in the through-thickness direction. Hence, the sheared edge profile is also not smooth for the coarse mesh model. With these results, mesh size at the trimmed region is kept as 20 µm in other FE models.

Meanwhile, meshes sizes of the FE models for the fracture tests analysis affect the calibration of the fracture model parameters during the hybrid numerical-experimental analysis. Most of the ductile fracture models (or damage models) are defined as a function of local variables——strains and stresses. For coupled damage models such as Gurson or continuum damage model (CDM), both global load-displacement behavior and local stresses and strains variables depend on the element size since stresses on the damaged material points are softened [46, 47]. For uncoupled fracture criteria such as Hosford-Coulomb or Mohr-Coulomb model, global behavior predicted by FE simulations are approximately independent, but the local stresses and strains are dependent on the mesh size at the critical region where fracture initiation occur [28, 34, 35]. For this reason, fine meshes are recommended in the FE simulations for the hybrid optimization of the fracture criteria. In this study, for all finite element models of the fracture tests, we set the critical element size as 5 µm for the in-plane length, and the number of layers in the thickness direction was 16 in the critical region. Meanwhile, non-local approaches can be used to avoid such an element size effect especially when the coupled damage models are used [48, 49].

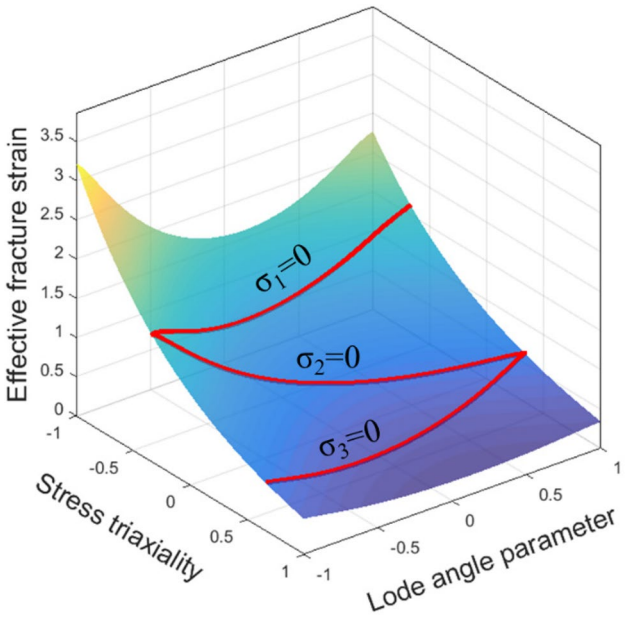

Fig. 5 Hosford-Coulomb fracture strain surface for DP980 sheet material

Results and discussion

Validation of the FE models under straight-cutting

In this section, 2D and 3D FE models of the trimming process in a straight-line path for DP980 material at 10% clearance condition were validated by comparing the experimental data. The predicted sheared edge, resulting from the 3D FE model, is shown in Fig. 8a with different zones of shearing. At the beginning of the trimming process, the punch pushes the blank from the top surface of the sheet into the clearance gap between the die and punch as it moves downward. The trimming process can be decomposed into three steps. The first step is the elastic stage where the punch contacts a sheet metal and deforms the blank elastically. At this step, small bending of the sheet is observed, and the length

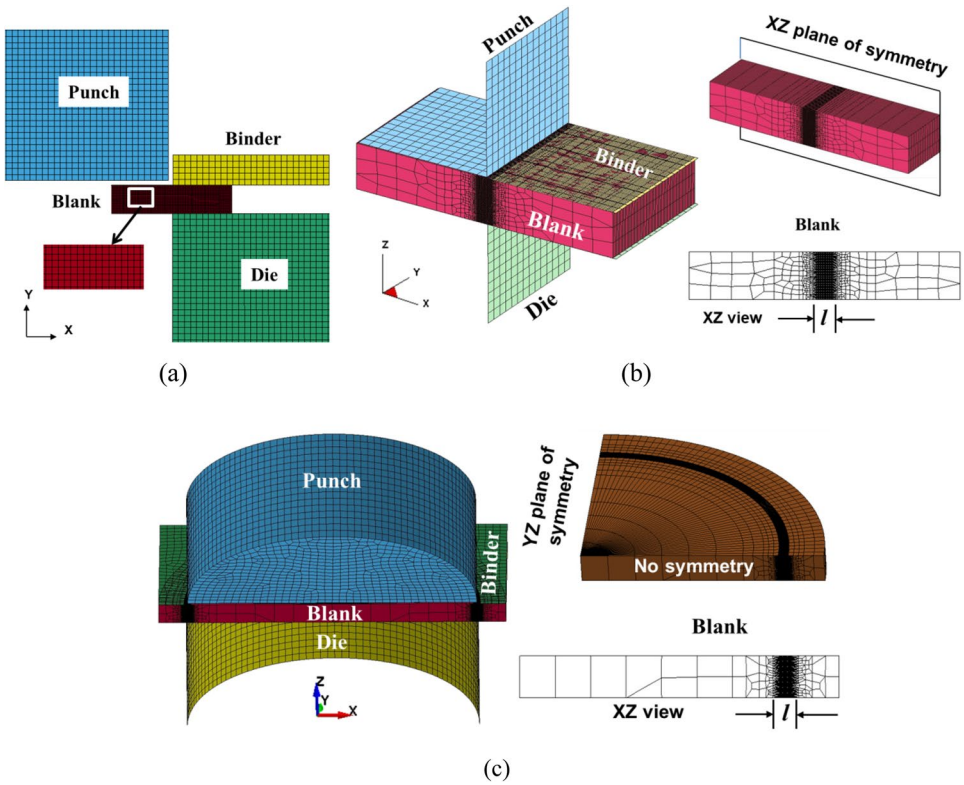

Fig. 6 **a** 2D and **b** 3D FE models for trimming in the straight-line path, and **c** 3D FE model for a circular path

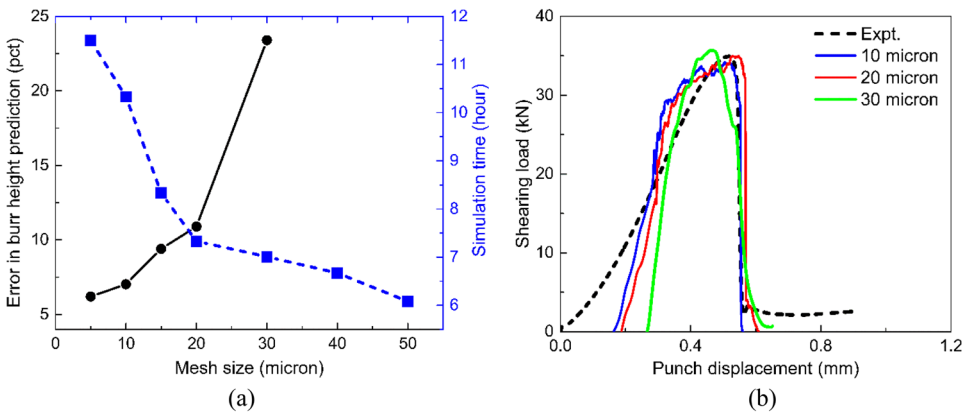

Fig. 7 Mesh size sensitivity analyses. **a** Burr height prediction error and **b** load-displacement curve predictions

of this top zone is referred to as the rollover zone as shown in Fig. 8. The second step is the elastic-plastic stage, where the punch starts to penetrate the blank gradually. In this step, the stresses in the blank quickly reach the yield strength of the material, and a plastic zone is formed between the punch and die at the clearance region. Further, as the damage indicator D reaches 1 with an accumulation of the plastic strain, initiation of the crack started. From the endpoint of the rollover up to the crack initiation point is referred to as the shear zone. After the initiation of the crack, it grows in size and propagates along with the shear band quickly with a downward movement of the punch. This results in the complete separation of the scrap from the blank via ductile fracture. The zone after the shear zone is termed as the fracture one as can be clearly shown in Fig. 8. The burr region is produced because of the intersection of the fractured surface of the blank in contact with the die. In summary, the length of each characteristic zone in FE simulations can be measured by tracking simulation results frame by frame.

The experimental shear profile along the through-thickness direction is shown in Fig. 8b. Also, numerically predicted shear profiles from 2D and 3D FE models are compared in Fig. 8c and d, respectively. It can be observed that both the 2D and 3D FE models can precisely predict the shape and geometrical features of the shear profile. Moreover, the predicted lengths of each characteristic zone are in good match with the experimental values.

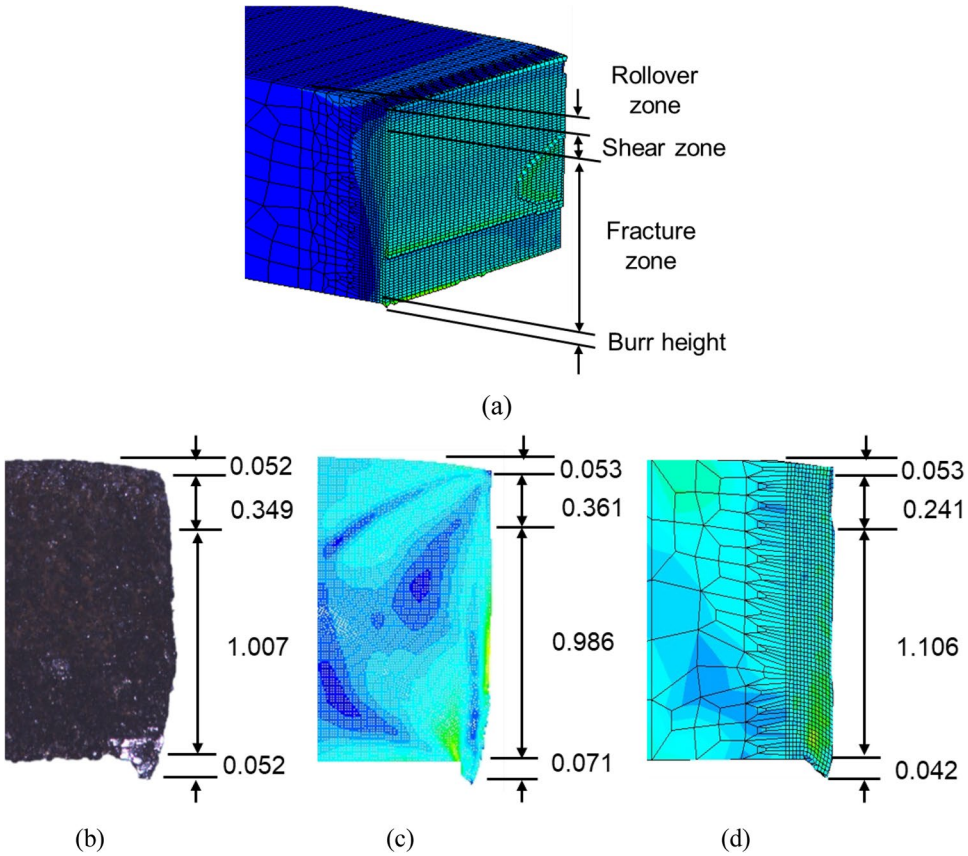

Fig. 8 **a** Different zones of shearing during trimming in a straight line path and comparison of trimmed surface profile quality with **b** experimental data and simulation data obtained from **c** 2D and **d** 3D trimming for DP steel at 10% clearance value (dimensions are in mm)

Further, the experimental load progression curve is compared with the predicted curves by both 2D and 3D models in Fig. 9. It can be observed that the load progression curves are predicted satisfactorily by both the 2D and 3D models. Moreover, the peak loads, estimated by both the FE simulations, are within an error margin of 5%. Hence, it can be concluded that both the 2D and 3D FE models are equally efficient to predict the trimming process in a straight-line cutting. However, in the real industrial application, the trimming process does not always follow the straight-line path; rather the process can be along a curvilinear path with a specified trimming angle. In such cases, 3D simulation is required to capture the actual deformation mode during trimming.

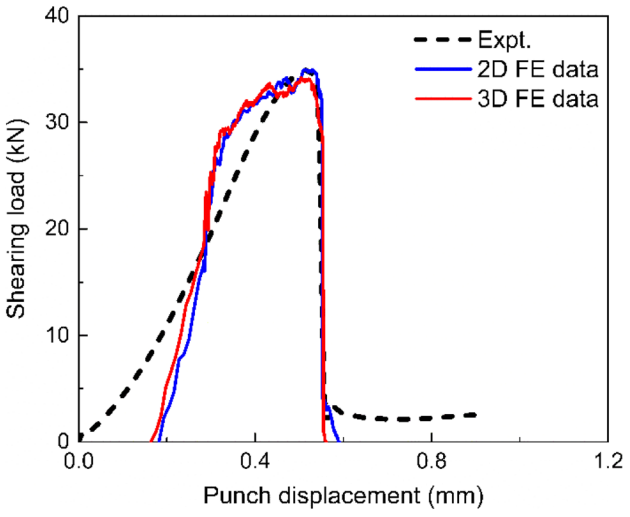

Fig. 9 Comparison of the load-displacement curves obtained from the experiment, 2D and 3D FE simulations

Effect of the trimming process parameters

After validating the FE model, virtual experiments are performed to understand the effect of individual process parameters on the trimming process. Among the various process parameters, three major parameters including trimming angle, clearance, and punch diameter in a circular path are considered in the present study.

Trimming angle

The effect of trimming angle on the straight trimming process is investigated with the help of virtual experiments. Three different trimming angles viz. 0°, 10°, and 20° are considered at a constant 10% clearance of DP980 sheet

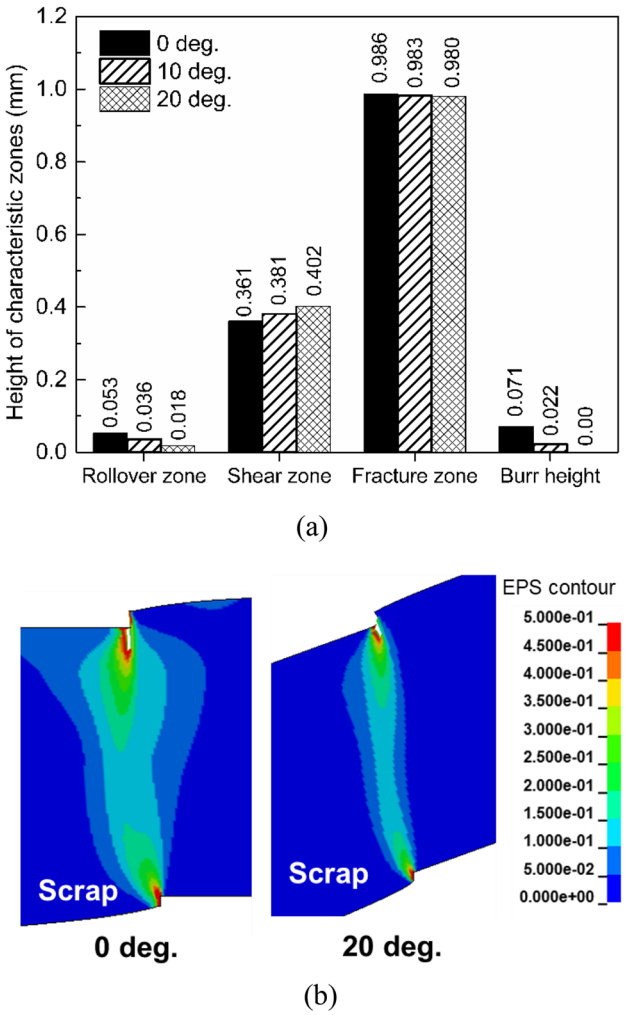

Fig. 10 **a** Influence of trimming angle on the quality of the sheared edge during the straight trimming of DP sheets at 10% clearance condition and **b** comparison of the EPS contour at the same punch displacement during inclined trimming

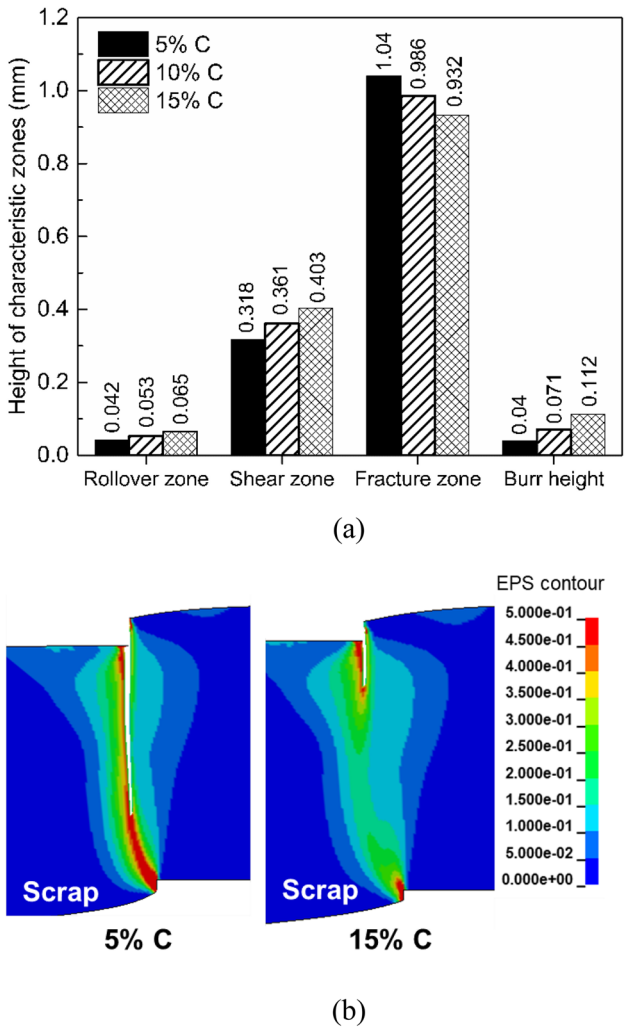

Fig. 11 **a** Influence of trimming clearance on the quality of the sheared edge for straight-line cutting at 0° inclination angle and **b** comparison of the EPS contour at the same punch displacement in 5% 15% C conditions

thickness. The heights of each of the characteristic zone are measured from the sheared edge and are compared in Fig. 10a. It can be observed that the rollover height decreases with the increasing trimming angle. This is due to the early penetration of the punch into the blank during trimming the inclined sheet metal. It can be also seen that the shear zone height increases with the increase in the inclination angle. For understanding the reason, the effective plastic strain (EPS) contours of the 0° and 20° trimming angle cases are compared at the same punch penetration depth in Fig. 10b. The EPS contour is comparatively narrower in the case of inclined trimming, which indicates a comparatively lesser bending moment is induced. During straight trimming (0° case), a bending moment occurs due to rotation of the scrap side which induces tensile stress at the crack tip. This bending moment increases the tensile stress at the crack tip towards the perpendicular direction to the shear zone along the punch movement direction. This phenomenon helps to propagate the crack developed quickly, and it induces the low shear zone height. On the other hand, the bending moment applied during the trimming is less due to less rotation of the scrap in the inclined trimming. Therefore, the crack development is delayed due to less accumulation of EPS. For this reason, the height of the shear zone of the trimming with a 20° inclination angle is 10.2% more compared to that of the straight trimming condition. Furthermore, the burr height decreases as the inclined angle increases. Practically, no burr is predicted for the 20° inclined trimming. Hence, it is recommended to use inclined trimming conditions to avoid burr formation in the real application of the DP980 sheets. The variation on the peak load was also analyzed for the difference in the inclined angles. The recorded peak loads

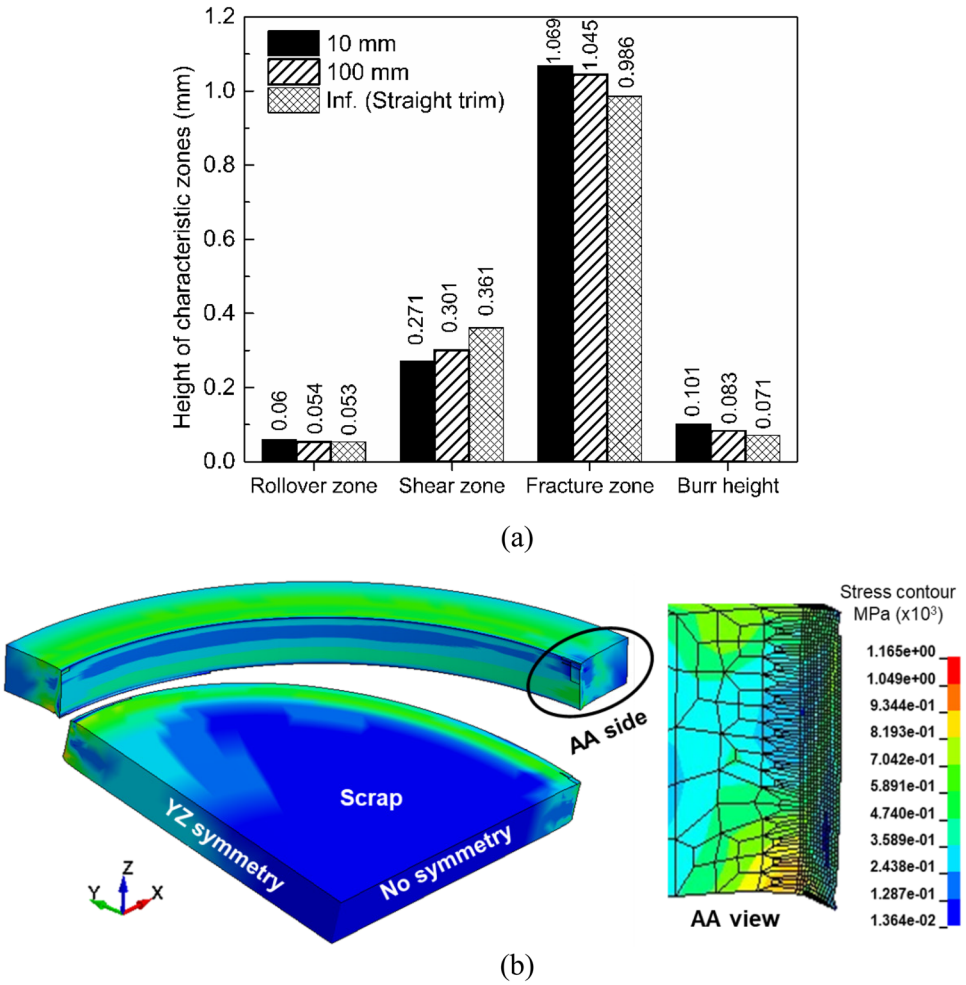

Fig. 12 **a** Influence of punch radius on the quality of the sheared edge during trimming of DP980 sheets at 0^0 trimming angle with 10% clearance condition and **b** the stress contour during trimming in a circular path

are 0.873 kN/mm, 0.862 kN/mm, and 0.854 kN/mm for trimming at an inclination angle of 0°, 10°, and 20°, respectively. A decrease in the peak load is observed with the increase in the inclination angle.

Trimming clearance

Virtual experiments at three different clearances viz. 5%, 10%, and 15% of the sheet thickness are carried out for straight trimming, and the heights of the characteristic zones are compared in Fig. 11a. It can be observed that the rollover zone, shear zone, and burr height increase as the clearance increases. This is because of the change in material flow which directly influences the stress state during deformation. During the trimming with larger clearance, the yield of the sheets is prolonged as the punch pushes a comparatively larger amount of the blank into the clearance region. For this reason, the rollover height increases by 20.7% and 35.4% for 10% and 15% clearance (hereafter, 5%, 10%, 15% C) compared to that of the 5% C condition. Further, the crack initiation is delayed because of the larger clearance which is responsible for larger shear zone height at 10% and 15% C as observed in Fig. 11a. To understand this, the EPS contour at two extreme clearances (5% and 15% C) are compared at the same punch travel as shown in Fig. 11b. It can be observed that the crack has been propagated to a larger depth with the same displacement of the punch for 5% C condition. This confirms the delay in crack initiation and propagation which leads to the higher rollover zone for larger clearance conditions. With larger rollover and shear zones, a more deformed blank wraps around the die corner, and it produces a larger amount of burr. For this reason, the burr heights are 43.6% and 64.3% more at 10% and 15% C conditions compared to that of the 5% C condition. Also, the clearance shows a significant variation in the peak load. The recorded peak loads are 0.894 kN/mm, 0.873 kN/mm and 0.832 kN/mm for trimming at 5%, 10% and 15% C conditions, respectively. The peak load is reduced in magnitude with an increase in clearance because the bending effect of the blank is more involved with increased clearance, which delays the occurrence of the peak load and initiation of the fracture.

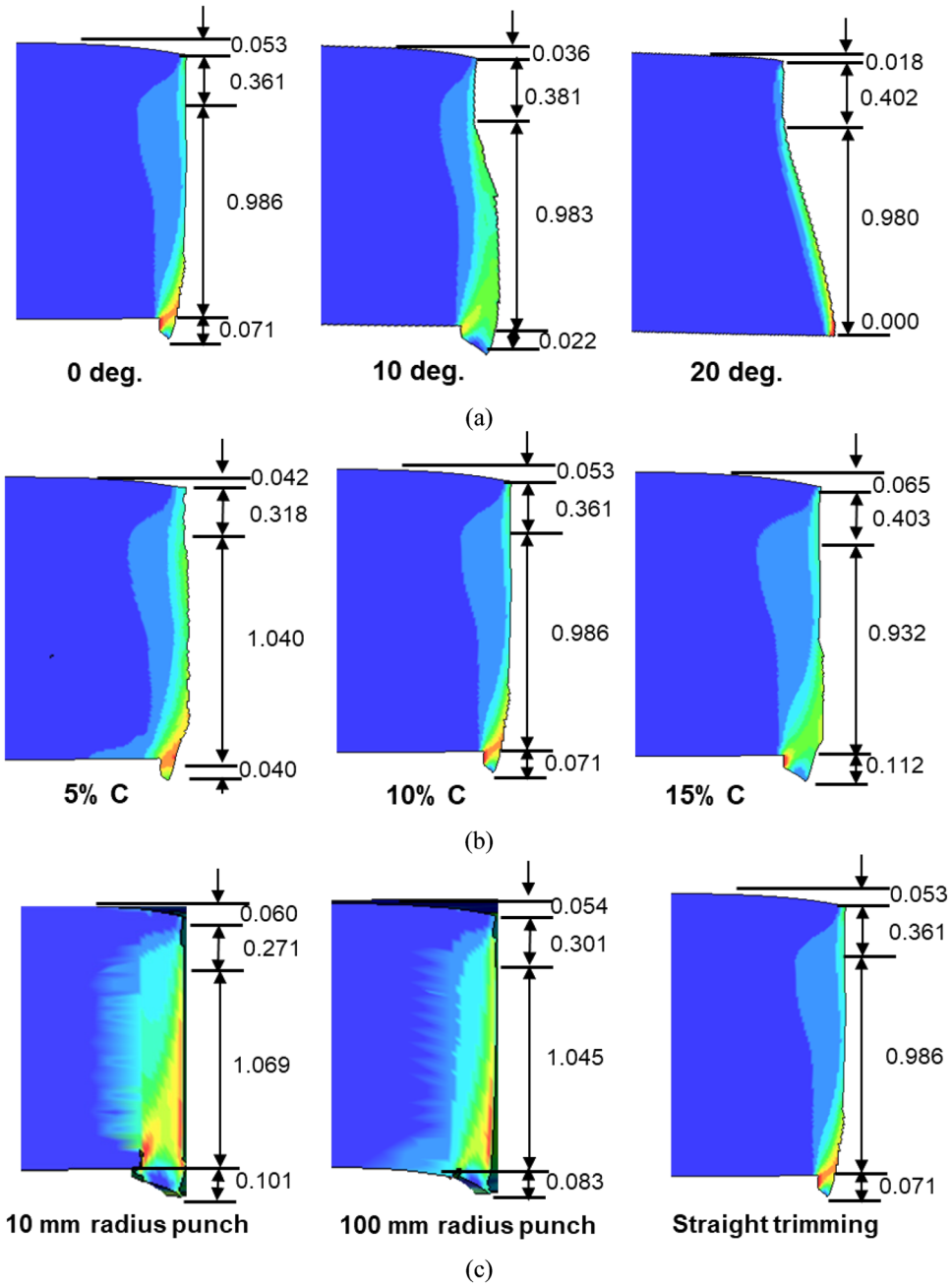

Fig. 13 Comparison of trimmed surface profiles obtained by varying (**a**) trimming angle, (**b**) trimming clearance and (**c**) punch radius (dimensions are in mm)

Punch radius

A stamped/deep drawn automotive component is often required trimming in a curvilinear path at the final stage. Hence, the effect of punch radius on the sheared edge quality is studied in this work. Three different punch radii viz. 10, 100 mm, and infinity (which is straight-cutting) are used to carry out the virtual trimming experiments at a

Table 3 List of Input process parameters with their ranges

Sl. No	Input parameters	Unit	Minimum value		Middle value		Maximum value	
			Un-coded	Coded	Un-coded	Coded	Un-coded	Coded
1	Trimming angle (A)	degree	0	−1	10	0	20	+1
2	Trimming clearance (C)	pct.	5		10		15	
3	Punch radius (R)	mm	10		100		Inf.	

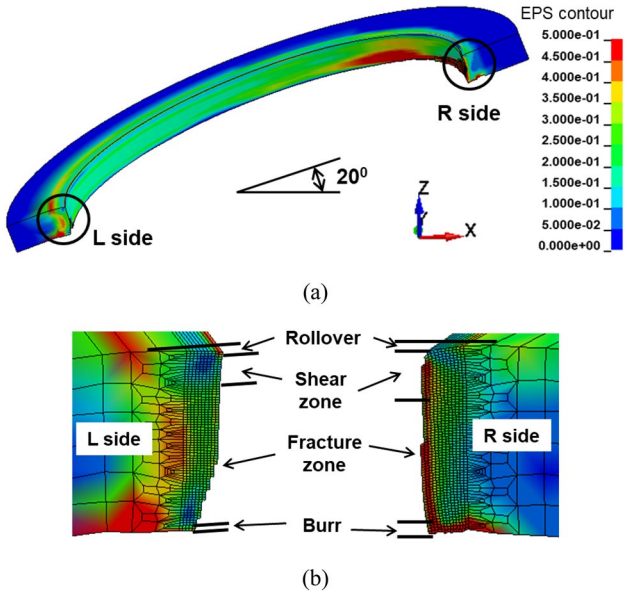

Fig. 14 **a** FE predicted trimmed surface during circular trimming with a punch radius of 10 mm at 20° inclination angle and **b** comparison of the left and right side trimmed edge profiles

constant inclination angle 0° and 10% clearance condition. The heights of each of the sheared zones are compared in Fig. 12a for three radii conditions. Modeling of trimming process with a circular punch required a 3D FE model as discussed previously.

The stress contour during trimming in a circular path is shown in Fig. 12b. It can be observed that the removal of scrap is not uniform along with the XZ and YZ planes as the boundary conditions are different in these two planes. Therefore, the sheared edge quality is also different along these two mutually perpendicular planes. Considering that the YZ plane is a symmetry plane, characteristic lengths of each zone for the comparative analysis are collected from the free edge at the AA side (on the XZ plane) as marked in Fig. 12b. It can be observed from Fig. 12a that the height of the rollover zone is tentatively the same for all the trimming conditions. However, the shear zone height is reduced by 24.9% during trimming with a 10 mm radius case compared to that of the straight trimming. It is because of the two different boundary conditions involved during trimming in a curvilinear path and straight path. During circular trimming, the rotation of the scrap is limited compared to that of the straight trimming, since the half-circular region around the trimmed area is clamped tightly during the trimming. Therefore, the accumulation of tensile stress at the crack tip and subsequent crack development is delayed. Due to the following reason, the shear zone height is largest while trimming with a circular punch of 10 mm radius. Also, during circular trimming, there is a tendency for the scrap to wrap around the die corner tip and this is the reason for high burr development. The recorded normalized peak loads are 0.878 kN/mm, 0.876 kN/mm, and 0.873 kN/mm for trimming with a punch radius 10, 100 mm, and straight-cut, respectively. The normalized peak load increases slightly because of the constrained boundary condition during circular trimming.

In Fig. 13a, b, and c, the sheared edge profiles for all the investigating cases are compared for varying trimming angle, clearance, and punch radius, respectively. In Fig. 13a, it can be observed that the cut edge profile becomes slant due to the inclined holding setup of the trimming process. Moreover, at the 20° inclination angle there is no burr formation as

Table 4 Design matrix with input and responses measured during trimming simulations

Run Order	Input process parameters			Response parameters		
	A (degree)	C (%)	R (mm)	S/F ratio	Peak load/unit length (kN/mm)	Burr height (mm)
1	20	5	100	0.319	0.883	0.000
2	20	15	100	0.340	0.829	0.038
3	10	5	10	0.285	0.877	0.062
4	0	10	10	0.254	0.878	0.101
5	20	10	10	0.326	0.864	0.01
6	0	5	100	0.266	0.914	0.046
7	0	15	100	0.292	0.847	0.102
8	10	5	inf	0.340	0.866	0.000
9	10	15	inf	0.389	0.803	0.087
10	10	10	100	0.301	0.832	0.058
11	0	10	inf	0.366	0.873	0.071
12	20	10	inf	0.410	0.854	0.000
13	10	10	100	0.301	0.832	0.058
14	10	10	100	0.301	0.832	0.058
15	10	15	10	0.354	0.815	0.112

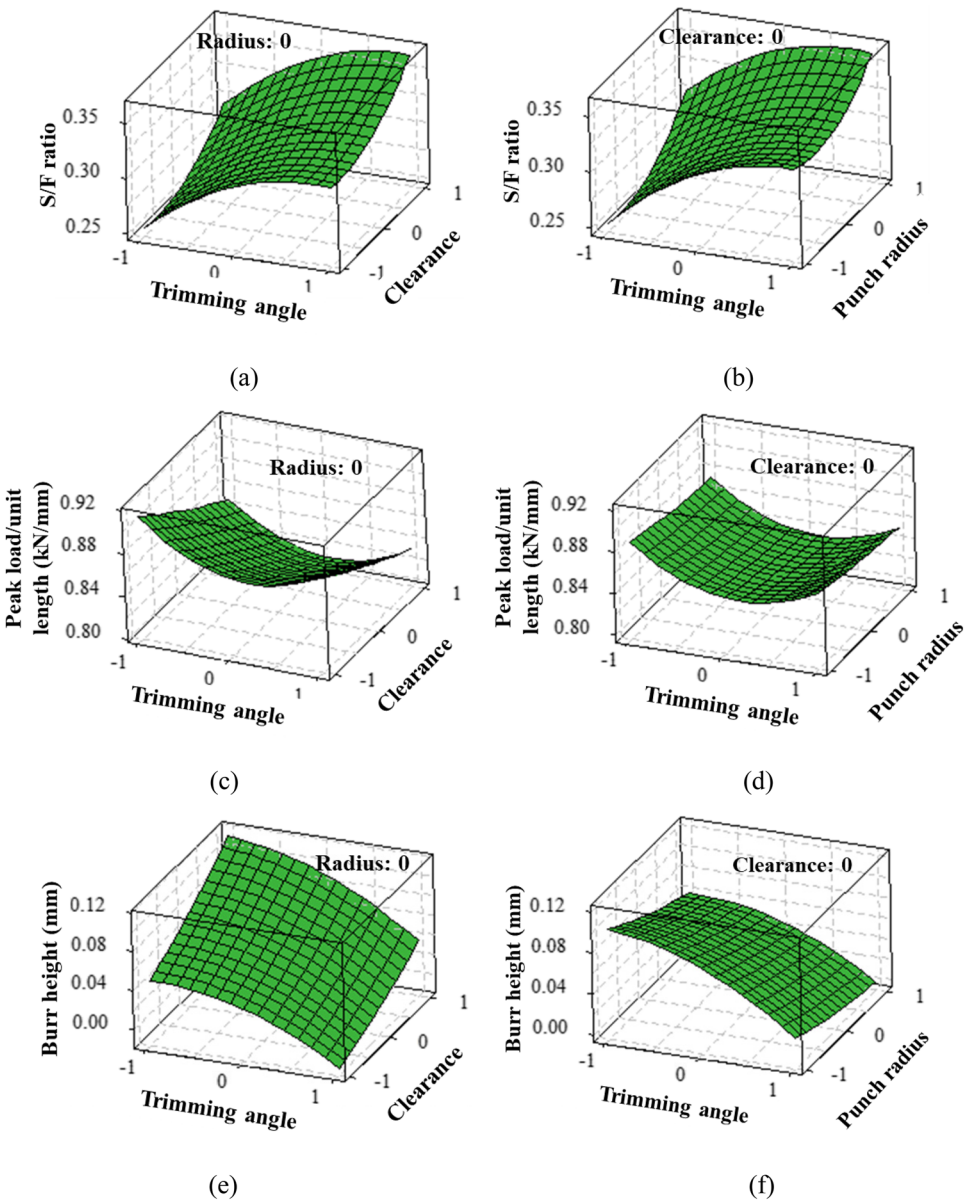

Fig. 15 Evaluated 3D Response surfaces based on predicted regression models for (**a**)-(**b**) S/F ratio (**c**)-(**d**) peak load per unit length and (**e**)-(**f**) burr height

depicted in the figure. Also, Fig. 13b clearly shown that the larger clearance induces the larger burr heights and width. The effect of punch radius on the sheared edge profile is shown in Fig. 13c. In Fig. 13c, the 3D shear surface profile is shown in XZ plane for trimming in a circular path with a punch radius of 10 mm and 100 mm. Compared to the straight trimming, a slight increase in the burr heights is observed in cases of circular punch trimming.

Regression models for the trimming process

In the above, the effects of process parameters are investigated on the trimming quality separately. In a practical scenario, all these process parameters can be varied simultaneously. On the other way, combinations of these process parameters together can improve the sheared edge quality of the ongoing trimming process. However, conducting FE simulations for each complex trimming process condition is a time-consuming job. Hence, in the present work, regression models are developed to correlate the trimming output parameters with the input process variables using the analyses of variance (ANOVA) technique. Furthermore, the correlations among the process parameters are successfully established with the help of the response surface methodology (RSM) technique implementing the Box-Behnken design (BBD) method. The regression equation (Y) for the

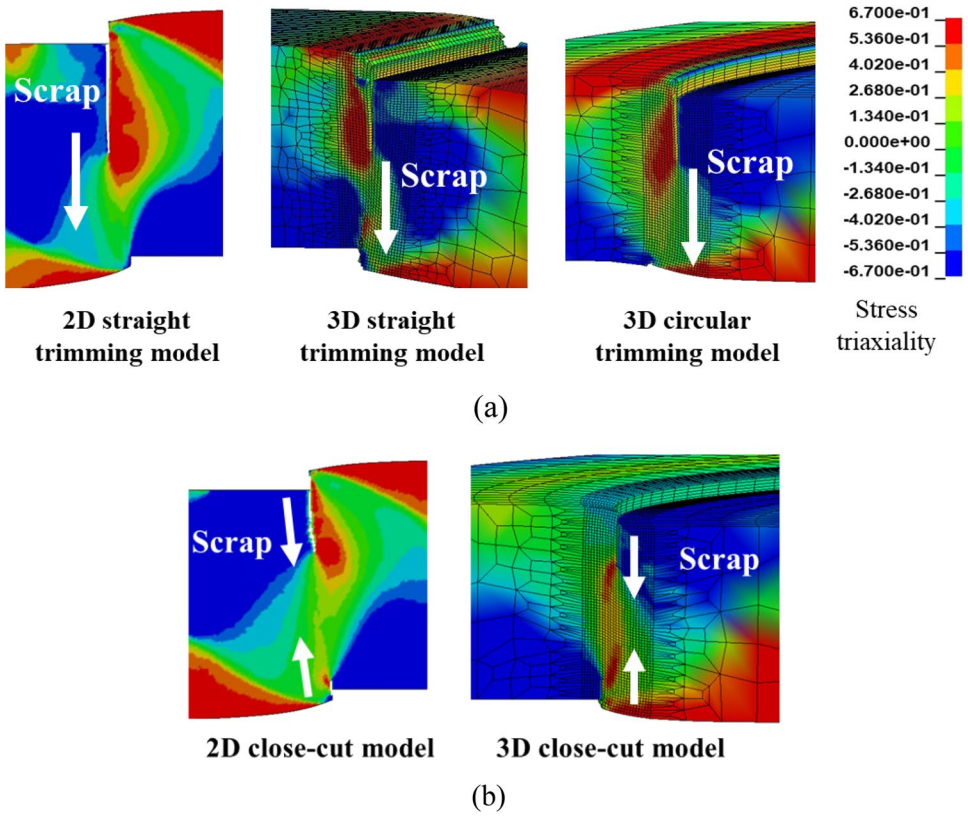

Fig. 16 Comparison of crack propagation path during (**a**) open-cut (trimming) and (**b**) close-cut (piercing) processes

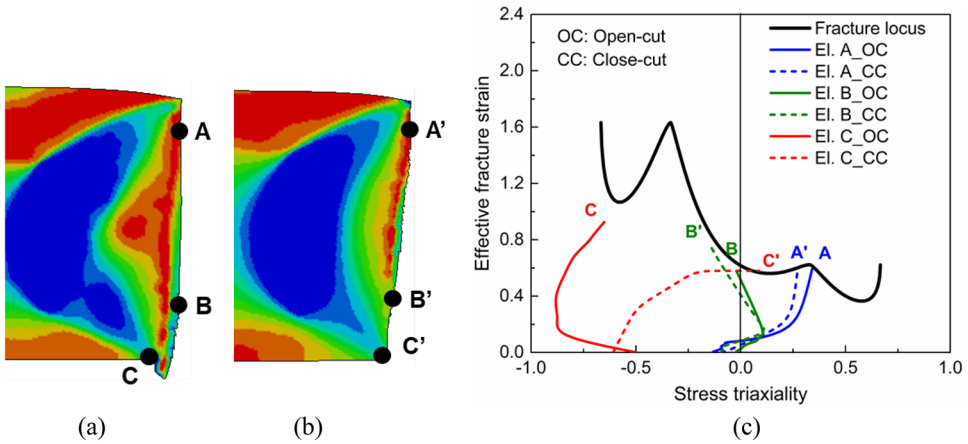

Fig. 17 Location of the elements within the trimmed part during (**a**) open-cut and (**b**) close-cut trimming along with the (**c**) evolution of stress triaxiality for these elements from different characteristics zones

response surface can be represented through a quadratic polynomial as shown in Eq. (10).

$$Y = \alpha_0 + \sum_{j=1}^{k} \alpha_j X_j + \sum_{i=1}^{k} \alpha_{jj} {X_j}^2 + \sum_{i=1}^{k-1} \sum_{j=i+1}^{k} \alpha_{ij} X_i X_j + E \qquad (10)$$

Here,α_i are the required regression coefficients that need to be evaluated based on trimming data set, and E represent a random error. Also, Y is the output parameter, and X is the independent input parameter. To identify the significant term in the regression model, the F ratio [17] and corresponding probability (p) values are used. Also, the coefficient of determination (R^2) value is evaluated from the statistical model to identify the goodness of the fit of the evaluated regression equations.

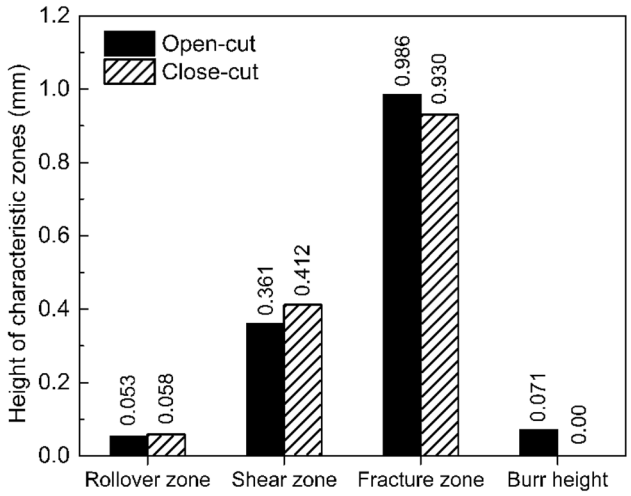

Fig. 18 Effect of open and close-cut trimming on the quality of the sheared edge

Trimming process input and response parameters

Among many process parameters that can affect the trimming quality, three parameters namely trimming angle (A), clearance (C), and punch radius (R) are considered in the present study. Hence, these three parameters are identified as the independent influencing parameters. Three different trimming angles of 0°, 10°, and 20° are considered. Similarly, three different clearance values of 5%, 10%, and 15% of the corresponding sheet thickness (1.4 mm) are considered. Finally, three different punch radii of 10 mm, 100 mm, and infinity (straight) are taken. All these real "un-coded" values are defined as relative "coded" values from −1 to 1 for the RSM analysis, and detailed conditions are summarized in Table 3. Further, the number of cases is selected as 15 with three central points for three factors-three levels BBD method. The regression analyses are performed using statistical software MINITAB using FE simulation results.

Three different responses such as shear to fracture zone height ratio (S/F ratio), peak load per unit length, and burr height are measured for each of the input cases from FE simulation results. S/F ratio indicates the amount of clean shear zone height w.r.t. the fracture zone height. As discussed previously, it can be observed that the shear zone height directly depends upon the shearing mechanism and the accumulation of the tensile stress at the crack tip that is related to the rotation of the scrap. Hence, a lesser S/F ratio shows the early development of the crack during trimming.

However, measurement of the S/F ratio is critical particularly during inclined trimming at a circular path as shown in Fig. 14a. It can be observed that during circular trimming, say at a trimming angle of 20° and 10% clearance condition, the trimmed edge profile of left (L) side and right (R) side are not equal. More clearly, an asymmetric sheared edge characteristic is obtained along the circumference of the trimming line. To emphasis this fact, the edge profiles for L and R sides are shown explicitly in Fig. 14b. A considerable difference is observed in both L and R side trimmed profiles. That is because of the bending moment induced during the trimming process. As the trimming starts from the R side, the scrap rotation is restricted at that side. Hence, there is a delay in the development of crack, and the shear zone height increases, whereas in the L side, the scrap is already near to be separated, and hence the tensile stress is high at the crack tip which induces quick development of the crack. Despite this difference, the average of the L and R side characteristic zone heights is adopted in this work for simplicity, and the S/R ratio is calculated subsequently.

Punching load during trimming is another important parameter as it is required to set an idea about the capacity of the press during the trimming process. However, in the present work, due to the geometry difference for the different conditions, the peak load varies during trimming in a straight and circular path. For a fair comparison, the peak load is normalized with the perimeter of the trimming region. Furthermore, the burr height is also a critical output parameter as it determines the quality of the trimmed product, and it is considered as the third output in the present regression study.

Estimated regression models

The output responses, obtained from the FE simulations, are listed in Table 4. These output variables are used to evaluate the regression coefficients of response surface in Eq. (10). Separate regression equations are developed for each output. The best-fitted regression models in terms of the input variables are shown in Eq. (11) after removing the insignificant terms. The coefficients of determination or R^2 values for S/F ratio, normalized peak load, and burr height cases are 0.9547, 0.9964, and 0.9531, respectively.

$$\begin{aligned} S/Fratio &= 0.301 + 0.031 \times D + 0.021 \times C + 0.021 \times R + 0.018 \times C^2 + 0.023 \times R^2 \\ load/unitlength &= 0.832 - 0.010 \times D - 0.030 \times C - 0.005 \times R + 0.031 \times D^2 \\ &\quad +0.005 \times C^2 + 0.004 \times R^2 + 0.003 \times D \times C \\ burrheight &= 0.058 - 0.034 \times D + 0.029 \times C - 0.016 \times R - 0.016 \times D^2 \end{aligned} \tag{11}$$

Based on the regression model in Eq. (11), response surfaces are presented in Fig. 15. The output responses are marked along Z-axis. Also, two input factors (as a coded value from −1 to 1) are represented as the X and Y axis, while the other remaining input is fixed as 0 (coded value). For example, in Fig. 15a, the S/F ratio is represented as Z-axis, and two input factors—trimming angle and clearance—are plotted along X and Y axes, respectively, while another input factor, punch radius was zero to calculate the surface in the figure. It is noteworthy to mention that

each 3D contour of Fig. 15 represents a combination of an infinite number of possible solutions of the two input factors on the respective output parameter.

From Fig. 15a, it can be understood that with the increase in trimming angle the S/F ratio increases i.e. shear zone height increases. However, the rate of increment of the S/F ratio is more for the 0–10° range compared to that of the 10 to 20° range. This indicates that the delay in the crack development is more within 0 to 10° inclination angle range. On the other hand, the increment of the S/F ratio is comparatively linear within the operating range of 5–15% clearance as depicted from Fig. 15a and b. Further, the shear zone height is steadily decreasing for using circular punch compared to straight trimming. Similarly, the decrement of the peak load per unit length is linear with increasing clearance, however, peak load is not varied much for changing punch radius. Linear decrement of the burr height is prominent with the increase in the trimming angle, on contrary, the burr height increases steadily with the increase in the clearance which is not desirable. Furthermore, the burr height also increases slightly for decreasing the radius of the punch. From this discussion, it is evident that too much clearance is not desirable as it increases the burr, on contrary, smaller clearance yields a higher peak load which is also not desirable from the manufacturing point of view. In other words, peak load and burr height have a trade-off relation for the clearance change. Meanwhile, using a small punch radius can yield a high amount of burr, which can be minimized by reducing the clearance value while taking care of the peak load of the press. Hence, it is understandable that the regression analyses and response surface is useful to improve the quality of sheared edge, and subsequently, designing the complex trimming process conditions with suitable process parameters.

Comparison between open-cut and close-cut

The present study is further extended to compare between the open-cut and close-cut shear-cutting processes. During the open-cut process, the shear cutting takes place along an open boundary line. For example, trimming along a straight or curvilinear line with an open edge (refer Fig. 2a), and this operation is generally called a notching process. However, during the close-cut process, the shear cutting takes place within a close boundary line. In industry, the close-cut process is known as punching or hole-piercing operation where the cutting edges are confined into the sheet materials.

The basic difference between the open and close-cut processes is the boundary condition. Similar to the open-cut FE model (2D and 3D), the close-cut FE model is also generated both in 2D and 3D space. 2D axisymmetric (as the process processes rotational symmetry along the Z axis) and the 3D hole-piercing FE models are developed separately with suitable boundary conditions in LS-Dyna for the close-cut model. The meshing scheme is kept the same as in the open-cut model as discussed. The hole-piercing experiments are virtually conducted with a 10 mm punch radius at 10% clearance condition and zero trimming angle.

Mechanism of crack development

The trimmed edges, generated from open-cut and close-cut processes, are compared in Fig. 16. The stress triaxiality contours of all open-cut FE models are compared in Fig. 16a at equal punch travel. The first thing that can be observed in the figures is that the stress triaxiality of the blank at the contact of the punch and die is negative (blue color) for high compression at the contact area. However, the stress triaxiality of the bottom part of the blank, which is yet to be trimmed, is almost zero (green color), and it corresponds to the shear stress states. During deformation, the plastic strain reaches the defined fracture strain, and a crack is initiated. With the continued downward movement of the punch, the scrap side starts rotating and results in the bending moment and tensile stress at the crack tip. Therefore, the stress triaxiality at the crack tip region is highly biaxial (red color), as shown in Fig. 16a. It can be noted that after the initiation of the crack, it grows in size and propagates along with the shear band quickly with a downward movement of the punch. This results in the complete separation of the scrap from the blank via ductile fracture.

A prominent difference in crack initiation and propagation mechanism is observed during open-cut and close-cut processes. As observed in Fig. 16a, during the open-cut process the crack is initiated from the top portion of the blank and propagated along the punch movement direction. This “single crack formation mechanism” is observed for all open-cut models including the 2D model, 3D straight trimming model, and 3D circular trimming model. However, for the close-cut process (Fig. 16b), cracks are generated from the both top (near the punch edge) and bottom (near the die edge) side, and propagated towards the inside of the materials. This “double crack formation mechanism” is observed for all close-cut models including the 2D axisymmetric model and 3D hole-piercing model. This gives a fairly smooth sheared surface without any prominent presence of burr formation. The main reason behind the formation of the “single crack formation mechanism” and “double crack formation mechanism” is the induced bending moment during the rotation of the scrap. For open-cut trimming, a considerable rotation of the scrap portion can be observed due to the unsupported boundary condition of the scrap. This extreme rotation of the scrap induces a huge bending moment and tensile stress at the crack tip. For this reason, a crack is immediately developed at the punch edge and subsequently

propagated quickly. However, during the close-cut process, the rotation of the scrap portion is very much limited due to the closed boundary condition of the scrap. For this reason, cracks are generated at the top and the bottom side of the blank, and they produce a clear shearing edge without a burr.

Evolution of stress triaxiality

The stress triaxiality evolution is further examined during open-cut and close-cut conditions. Three elements from different characteristics shear zones are selected as shown in Fig. 17a (2D straight trimming FE model) and Fig. 17b (2D axisymmetric FE model). Element A (and A') present near the upper edge, and it represents the shear zone. Element B (and B′) and C (and C′) are selected from the fracture zone and the blank-die contact region, respectively. The evolution of the effective plastic strain with the stress triaxiality histories of these three elements is extracted from FE simulations and plotted with different colors in Fig. 17c. The solid and dotted lines correspond to open-cut and close-cut processes, respectively. Also, the plane stress fracture locus of the DP980 material is plotted in the same figure to understand the fracture initiation step during deformation. Both for the element A(open-cut) and A'(close-cut), the stress triaxiality represents the pure shear at the beginning of the deformation. However, with deformation, the triaxiality tends to shifts towards the positive triaxiality side, and the element ultimately fails with triaxiality around the uniaxial tensile state. It is because the initial penetration starts at the pure shear state; however, after some deformation, the scrap side starts rotating and induces a positive stress triaxiality at the crack tip. The maximum stress triaxiality at the positive side is less for close-cut trimming due to lesser scrap rotation which induces a lesser amount of bending moment and tensile stress into the material. It is observed that the stress triaxiality of element B/B′ shifts in the positive region initially but moves to the pure shear state during the failure. Owing to the rotation of the scrap, the triaxiality is positive at the initial state. However, after the accumulation of the damage, the fracture propagates rapidly, and the triaxiality state is nearly pure shear as can be observed for element B or B′. Contrary to the cases of the A/A' and B/B′, a massive difference can be observed in the triaxiality histories for the elements C and C′. Element C did not fail during deformation because it directly contacts the die surface, which results in compression during the trimming process or in negative triaxiality, and fracture strain generally smaller for the negative stress triaxiality. On contrary, element C′ is initially under compression and its triaxiality state is highly negative. With deformation, due to restricted scrap rotation, a bending moment is also generated at the die-blank interface, and therefore the triaxiality state immediately tends to shift from the high compressive region to the tensile region. As the triaxiality state touches the fracture curve of DP980 material, at that moment a crack front is generated from the die-black interface and subsequently propagated. This is the reason behind the "two crack formation mechanism" during the close-cut process of DP980 material.

Comparison of the shear surface quality

Heights of different characteristic zones are measured from the FE simulation and compared in Fig. 18. No significant difference can be observed in the rollover zone height. However, for the close-cut process, the shear zone height is around 12.4% more compared to the open-cut conditions. This is because the less bending moment is induced due to the limited rotation of scrap for the closed boundary condition. Therefore, the crack development is delayed due to less accumulation of tensile stress at the crack tip. This phenomenon extends the shear zone height for the close-cut condition of DP980 material. Due to which the fracture zone height is reduced during the close-cut process. Furthermore, the two simultaneous cracks are developed from the bottom and top interfaces, and hence no trace of burr can be observed during trimming in a close-line path as observed from Fig. 18. The recorded peak loads are recorded from the simulation and subsequently normalized with the cutting perimeter. The evaluated peak loads per unit length are 0.873 kN/mm, and 0.885 kN/mm for close-cut and open-cut trimming conditions, respectively. This indicates that there is not much variation in the load exerted in two different processes.

In summary, a significant difference in terms of the shearing mechanism is observed for two different processes for DP980 sheet material. As a result of which, the shear surface characteristics are quite different. However, it can be noted that the shearing surface characteristics also depend upon the material properties. Therefore, not only that different processes yield different shearing mechanism but also changing process parameters can yield different shearing mechanisms for some materials.

Conclusions

In this work, sheared edge quality of the DP980 material was investigated during the sheet trimming process implementing the calibrated HC ductile damage model. The effects of various process parameters on the shearing process were studied thoroughly. Detailed virtual experiments were performed using FE simulation for a closer observation on the variation of the shearing mechanism obtained from different trimming conditions. Moreover,

regression models were developed to correlate the sheared edge characteristics and trimming load with the input process variables such as trimming angle, clearance, and punch radius. Finally, the shearing mechanism and stress triaxiality evolution were compared for open-cut and close-cut processes. Following are the major conclusions obtained from the present analyses.

- The sheared edge quality was greatly affected by the process parameters including trimming angle, clearance, and punch radius. It was found that the shear zone height increased with the increase in the inclination angle and trimming clearance. However, the shear zone height decreased for using the circular punch. Also, the burr height decreased significantly with the increase in the inclination angle, whereas the burr height increased with the increase in clearance. The burr height increased for the circular trimming. These differences were due to the two different boundary conditions involved during trimming in a curvilinear path and straight path.
- Three different regression models were evaluated to correlate the sheared edge characteristics (in terms of S/F ratio and burr height) and a trimming load of DP980 material with the input process variables including trimming angle, clearance, and punch radius. Subsequently, these regression models were represented as 3D response surfaces. The graphical representations are convenient to visualize the tendency of variations of the process parameters on the outputs over the variation range. Furthermore, these models can be useful to calibrate the complex trimming process parameters in the process design.
- Two different crack propagation mechanisms viz. single crack formation mechanism and double crack formation mechanism were observed during open-cut and close-cut trimming, respectively, due to the difference in boundary conditions regarding the rotation of the scrap. Therefore, a strong difference in the stress triaxiality evolution was observed between the two cases. For open-cut trimming, the element in the die contact region did not fail because of the compressive stress at the die contact region, and this helped delay crack initiation. However, during close-cut trimming, the bending moment was generated at the die-blank interface due to restricted scrap rotation. Therefore, the stress triaxiality immediately tended to shift from the high compressive region to the tensile region, and a crack front was generated from the die-black interface.

Acknowledgments The present work has been supported by Hyundai Motor Company, which is greatly appreciated by all authors. Also, parts of the paper were based on the results from KEIT (No. 20010717) and NRF (Grant No. 2019R1A5A6099595 (ERC) and 2020R1A2B5B01097417). C. Kim appreciates the program of CRÈME supported by KIAT (No. P0002019).

Declarations

Conflict of interest The authors declare that they have no conflict of interest.

References

1. Golovashchenko SF, Wang N, Le Q (2019) Trimming and sheared edge stretchability of automotive 6xxx aluminum alloys. J Mater Process Technol 264:64–75. https://doi.org/10.1016/j.jmatprotec.2018.09.001
2. Hu XH, Sun X, Golovashchenko SF (2016) An integrated finite element-based simulation framework: from hole piercing to hole expansion. Finite Elem Anal Des 109:1–13. https://doi.org/10.1016/j.finel.2015.09.005
3. Golovashchenko S, Zhou W, Nasheralahkami S, Wang N (2017) Trimming and sheared edge Stretchability of light weight sheet metal blanks. Procedia Eng 207:1552–1557. https://doi.org/10.1016/j.proeng.2017.10.1077
4. Feistle M, Koslow I, Krinninger M et al (2017) Reduction of Burr formation for conventional shear cutting of boron-alloyed sheets through focused heat treatment. Procedia CIRP 63:493–498. https://doi.org/10.1016/j.procir.2017.03.161
5. He J, Li S, Dong L (2020) Experiments and FE simulation of edge cracking considering prehardening after blanking process. Int J Mater Form 13:547–560. https://doi.org/10.1007/s12289-019-01491-6
6. Habibi N, Beier T, Richter H, et al (2019) The effects of shear affected zone on edge crack sensitivity in dual-phase steels. In: IOP Conference Series: Materials Science and Engineering. 651: 12073.
7. Krinninger M, Steinlehner F, Opritescu D et al (2017) On the influence of different parameters on the characteristic cutting surface when shear cutting aluminum. Procedia CIRP 63:230–235. https://doi.org/10.1016/j.procir.2017.03.156
8. Mori K ichiro, Abe Y, Suzui Y (2010) Improvement of stretch flangeability of ultra high strength steel sheet by smoothing of sheared edge. J Mater Process Technol 210:653–659. https://doi.org/10.1016/j.jmatprotec.2009.11.014
9. Dalloz A, Besson J, Gourgues-Lorenzon AF et al (2009) Effect of shear cutting on ductility of a dual phase steel. Eng Fract Mech 76:1411–1424. https://doi.org/10.1016/j.engfracmech.2008.10.009
10. Li M (2000) Experimental investigation on cut surface and burr in trimming aluminum autobody sheet. Int J Mech Sci 42:889–906. https://doi.org/10.1016/S0020-7403(99)00033-8
11. Atkins AG (1990) On the mechanics of guillotining ductile metals. J Mater Process Technol 24:245–257
12. Xu J, Guo B, Wang C, Shan D (2012) Blanking clearance and grain size effects on micro deformation behavior and fracture in micro-blanking of brass foil. Int J Mach Tools Manuf 60:27–34. https://doi.org/10.1016/j.ijmachtools.2012.04.001
13. Choi HS, Kim BM, Ko DC (2014) Effect of clearance and inclined angle on sheared edge and tool failure in trimming of DP980 sheet. J Mech Sci Technol 28:2319–2328. https://doi.org/10.1007/s12206-014-0522-7
14. Chumrum P, Koga N, Premanond V (2015) Experimental investigation of energy and punch wear in piercing of advanced high-strength steel sheet. Int J Adv Manuf Technol 79:1035–1042

15. So H, Faßmann D, Hoffmann H et al (2012) An investigation of the blanking process of the quenchable boron alloyed steel 22MnB5 before and after hot stamping process. J Mater Process Technol 212:437–449. https://doi.org/10.1016/j.jmatprotec.2011.10.006
16. Mori K, Maeno T, Fuzisaka S (2012) Punching of ultra-high strength steel sheets using local resistance heating of shearing zone. J Mater Process Technol 212:534–540. https://doi.org/10.1016/j.jmatprotec.2011.10.021
17. Basak S, Prasad KS, Sidpara AM, Panda SK (2019) Single point incremental forming of AA6061 thin sheet: calibration of ductile fracture models incorporating anisotropy and post forming analyses. Int J Mater Form 12:623–642
18. Alaswad A, Olabi AG, Benyounis KY (2011) Integration of finite element analysis and design of experiments to analyse the geometrical factors in bi-layered tube hydroforming. Mater\& Des 32:838–850
19. Schenek A, Liewald M (2021) Punching with a slant angle-cutting surface quality. Esaform 2021. https://doi.org/10.25518/esaform21.455
20. Basak S, Panda SK (2018) Implementation of Yld96 anisotropy plasticity theory for estimation of polar effective plastic strain based failure limit of pre-strained thin steels. Thin-Walled Struct 126:26–37. https://doi.org/10.1016/j.tws.2017.04.015
21. Taupin E, Breitling J, Wu WT, Altan T (1996) Material fracture and burr formation in blanking results of FEM simulations and comparison with experiments. J Mater Process Technol 59:68–78. https://doi.org/10.1016/0924-0136(96)02288-1
22. Wai Myint P, Hagihara S, Tanaka T et al (2017) Determination of the values of critical ductile fracture criteria to predict fracture initiation in punching processes. J Manuf Mater Process 1:12. https://doi.org/10.3390/jmmp1020012
23. Marouani H, Aguir H (2012) Identification of material parameters of the Gurson--Tvergaard--Needleman damage law by combined experimental, numerical sheet metal blanking techniques and artificial neural networks approach. Int J Mater Form 5:147–155
24. Han X, Yang K, Ding Y et al (2016) Numerical and experimental investigations on mechanical trimming process for hot stamped ultra-high strength parts. J Mater Process Technol 234:158–168. https://doi.org/10.1016/j.jmatprotec.2016.03.025
25. Wang C, Chen J, Xia C et al (2014) A new method to calculate threshold values of ductile fracture criteria for advanced high-strength sheet blanking. J Mater Eng Perform 23:1296–1306. https://doi.org/10.1007/s11665-013-0861-z
26. Mohr D, Marcadet SJ (2015) Micromechanically-motivated phenomenological Hosford – coulomb model for predicting ductile fracture initiation at low stress triaxialities. Int J Solids Struct 68:40–55. https://doi.org/10.1016/j.ijsolstr.2015.02.024
27. Hu Q, Li X, Han X, Chen J (2017) A new shear and tension based ductile fracture criterion: modeling and validation. Eur J Mech 66:370–386
28. Lou Y, Huh H (2013) Prediction of ductile fracture for advanced high strength steel with a new criterion: experiments and simulation. J Mater Process Technol 213:1284–1302
29. Caro LP, Schill M, Haller K et al (2020) Damage and fracture during sheet-metal forming of alloy 718. Int J Mater Form 13:15–28
30. Basak S, Panda SK (2019) Necking and fracture limit analyses of different pre-strained sheet materials in polar effective plastic strain locus using Yld2000-2d yield model. J Mater Process Tech 267:289–307. https://doi.org/10.1016/j.jmatprotec.2018.10.004
31. Kim C, Min KM, Choi H, Kim HJ, Lee MG (2021) Development of analytical strength estimator for self-piercing rivet joints through observation of finite element simulations. Int J Mech Sci 202–203:106499. https://doi.org/10.1016/j.ijmecsci.2021.106499
32. Samadian P, ten Kortenaar L, Omer K et al (2020) Fracture characterization of tailored Usibor®1500-AS and damage modelling based on a coupled-micromechanical-phenomenological strategy. Eng Fract Mech 223:106785
33. Basak S, Panda SK (2019) Failure strains of anisotropic thin sheet metals : experimental evaluation and theoretical prediction. Int J Mech Sci 151:356–374. https://doi.org/10.1016/j.ijmecsci.2018.10.065
34. Dunand M, Mohr D (2010) Hybrid experimental-numerical analysis of basic ductile fracture experiments for sheet metals. Int J Solids Struct 47:1130–1143. https://doi.org/10.1016/j.ijsolstr.2009.12.011
35. Luo M, Dunand M, Mohr D (2012) Experiments and modeling of anisotropic aluminum extrusions under multi-axial loading - part II: ductile fracture. Int J Plast 32–33:36–58. https://doi.org/10.1016/j.ijplas.2011.11.001
36. Roth CC, Mohr D (2016) Ductile fracture experiments with locally proportional loading histories. Int J Plast 79:328–354. https://doi.org/10.1016/j.ijplas.2015.08.004
37. Gu G, Mohr D (2015) Anisotropic Hosford--Coulomb fracture initiation model: Theory and application. Eng Fract Mech 147:480–497
38. Marcadet SJ, Mohr D (2015) Effect of compression-tension loading reversal on the strain to fracture of dual phase steel sheets. Int J Plast 72:21–43. https://doi.org/10.1016/j.ijplas.2015.05.002
39. Pack K, Mohr D (2017) Combined necking & fracture model to predict ductile failure with shell finite elements. Eng Fract Mech 182:32–51. https://doi.org/10.1016/j.engfracmech.2017.06.025
40. Lou Y, Chen L, Clausmeyer T et al (2017) Modeling of ductile fracture from shear to balanced biaxial tension for sheet metals. Int J Solids Struct 112:169–184. https://doi.org/10.1016/j.ijsolstr.2016.11.034
41. Neukamm F, Feucht M, Haufe A (2008) Consistent damage modelling in the process chain of forming to crashworthiness simulations. LS-DYNA Anwenderforum 30:11–20
42. Andrade FXC, Feucht M, Haufe A, Neukamm F (2016) An incremental stress state dependent damage model for ductile failure prediction. Int J Fract 200:127–150. https://doi.org/10.1007/s10704-016-0081-2
43. Basak S, Panda SK, Lee MG (2020) Formability and fracture in deep drawing sheet metals: extended studies for pre-strained anisotropic thin sheets. Int J Mech Sci 170:105346. https://doi.org/10.1016/j.ijmecsci.2019.105346
44. Mattiasson K, Jergéus J, Dubois P (2014) On the prediction of failure in metal sheets with special reference to strain path dependence. Int J Mech Sci 88:175–191. https://doi.org/10.1016/j.ijmecsci.2014.08.006
45. Hallquist JO, others (2007) LS-DYNA keyword user's manual. Livermore Softw Technol Corp 970:299–800
46. Kiran R, Khandelwal K (2014) Gurson model parameters for ductile fracture simulation in ASTM A992 steels. Fatigue\& Fract Eng Mater \& Struct 37:171–183
47. Oh Y-R, Nam H-S, Kim Y-J, Miura N (2018) Application of the GTN model to ductile crack growth simulation in through-wall cracked pipes. Int J Press Vessel Pip 159:35–44
48. de Sá JMAC, Areias PMA, Zheng C (2006) Damage modelling in metal forming problems using an implicit non-local gradient model. Comput Methods Appl Mech Eng 195:6646–6660
49. Park J, Lee K, Kang J-H et al (2021) Hierarchical microstructure based crystal plasticity-continuum damage mechanics approach: model development and validation of rolling contact fatigue behavior. Int J Plast 143:103025. https://doi.org/10.1016/j.ijplas.2021.103025